J|A|C|S
ARTICLES

Published on Web 08/05/2009

Trends in Covalency for d- and f-Element Metallocene Dichlorides Identified Using Chlorine K-Edge X-ray Absorption Spectroscopy and Time-Dependent Density Functional Theory

Stosh A. Kozimor,[†] Ping Yang,[†,‡] Enrique R. Batista,[†] Kevin S. Boland,[†] Carol J. Burns,[†] David L. Clark,*[,†] Steven D. Conradson,*[,†] Richard L. Martin,*[,†] Marianne P. Wilkerson,[†] and Laura E. Wolfsberg[†]

Los Alamos National Laboratory, Los Alamos, New Mexico 87545, and W.R. Wiley Environmental Molecular Sciences Laboratory, Pacific Northwest National Laboratory, Richland, Washington 99352

Received February 28, 2009; E-mail: dlclark@lanl.gov

Abstract: We describe the use of Cl K-edge X-ray absorption spectroscopy (XAS) and both ground-state and time-dependent hybrid density functional theory (DFT) to probe the electronic structure and determine the degree of orbital mixing in M−Cl bonds for $(C_5Me_5)_2MCl_2$ (M = Ti, **1**; Zr, **2**; Hf, **3**; Th, **4**; U, **5**), where we can directly compare a class of structurally similar compounds for d- and f-elements. Pre-edge features in the Cl K-edge XAS data for the group IV transition-metals **1**−**3** provide direct evidence of covalent M−Cl orbital mixing. The amount of Cl 3p character was experimentally determined to be 25%, 23%, and 22% per M−Cl bond for **1**−**3**, respectively. For actinides, we find a pre-edge shoulder for **4** (Th) and distinct and weak pre-edge features for U, **5**. The amount of Cl 3p character was determined to be 9% for **5**, and we were unable to make an experimental determination for **4**. Using hybrid DFT calculations with relativistic effective core potentials, the electronic structures of **1**−**5** were calculated and used as a guide to interpret the experimental Cl K-edge XAS data. For transition-metal compounds **1**−**3**, the pre-edge features arise due to transitions from Cl 1s electrons into the 3d-, 4d-, and 5d-orbitals, with assignments provided in the text. For Th, **4**, we find that 5f- and 6d-orbitals are nearly degenerate and give rise to a single pre-edge shoulder in the XAS. For U, **5**, we find the 5f- and 6d-orbitals fall into two distinct energy groupings, and Cl K-edge XAS data are interpreted in terms of Cl 1s transitions into both 5f- and 6d-orbitals. Time-dependent DFT was used to calculate the energies and intensities of Cl 1s transitions into empty metal-based orbitals containing Cl 3p character and provide simulated Cl K-edge XAS spectra for **1**−**4**. For **5**, which has two unpaired 5f electrons, simulated spectra were obtained from transition dipole calculations using ground-state Kohn−Sham orbitals. To the best of our knowledge, this represents the first application of Cl K-edge XAS to actinide systems. Overall, this study allows trends in orbital mixing within a well-characterized structural motif to be identified and compared between transition-metals and actinide elements. These results show that the orbital mixing for the d-block compounds slightly decreases in covalency with increasing principal quantum number, in the order Ti > Zr ≈ Hf, and that uranium displays approximately half the covalent orbital mixing of transition elements.

Introduction

The transition elements have been broadly defined as those elements that have partially filled d- or f-shell orbitals in any of their commonly occurring oxidation states and include the main transition or d-block elements, the lanthanide or 4f-block elements, and the actinide or 5f-block elements.[1] For d-block elements, the 3d-, 4d-, and 5d-orbitals extend well into the periphery of the atom and can interact with valence orbitals of ligand atoms to form covalent chemical bonds. In contrast, the 4f-orbitals of lanthanide elements are very corelike, and their interactions with ligands are of comparatively little chemical consequence.[2] The actinide elements lie between these two extremes, and there has been much debate over the ability of these elements to use either the 5f- or 6d-orbitals, or both, in chemical bonding interactions.[3−17]

[†] Los Alamos National Laboratory.
[‡] Pacific Northwest National Laboratory.

(1) Cotton, F. A.; Wilkinson, G.; Murillo, C. A.; Bochmann, M. *Advanced Inorganic Chemistry*, 6th ed.; John Wiley and Sons, Inc.: New York, 1999; pp 633−635.
(2) Crosswhite, H. M.; Crosswhite, H.; Carnall, W. T.; Paszek, A. P. *J. Chem. Phys.* **1980**, *72*, 5103.
(3) Glueckauf, E.; McKay, H. A. C. *Nature* **1950**, *165*, 594.
(4) Katzin, L. I. *Nature* **1950**, *166*, 605.
(5) Street, K., Jr.; Seaborg, G. T. *J. Am. Chem. Soc.* **1950**, *72*, 2790.
(6) Baker, E. C.; Halstead, G. W.; Raymond, K. N. *Struct. Bonding (Berlin)* **1976**, *25*, 23.
(7) Raymond, K. N.; Eigenbrot, C. W., Jr. *Acc. Chem. Res.* **1980**, *13*, 276.
(8) Iversen, B. B.; Larsen, F. K.; Pinkerton, A. A.; Martin, A.; Darovsky, A.; Reynolds, P. A. *Inorg. Chem.* **1998**, *37*, 4559.
(9) Choppin, G. R. *J. Alloys Compd.* **2002**, *344*, 55.

To evaluate trends in metal and ligand orbital mixing as a function of 3d, 4d, 5d, and 6d/5f metal orbitals, we report a comparative analysis of bonding in transition-metal and actinide bis(pentamethylcyclopentadienyl) dichloride compounds, $(C_5Me_5)_2MCl_2$ (M = Ti, **1**;[18] Zr, **2**;[19] Hf, **3**;[20] Th, **4**;[21,22] U, **5**[21,22]). This series was carefully selected for study since it provides a unique family of structurally similar compounds with which to evaluate trends in metal and Cl orbital mixing down the series of 3d-, 4d-, 5d-, and 6d/5f-elements. The $C_5Me_5^-$ system is important in this comparison since the $(C_5H_5)_2MCl_2$ framework does not provide stable actinide compounds.[23,24] Moreover, the bent metallocene dichlorides are among the most extensively utilized systems in organometallic research.[25−36] They are the foundational models of bonding and electronic structure in a large family of bent metallocenes that have had widespread use in catalysis,[25−32] in synthetic chemistry,[33,34] as antitumor agents,[35] and as models for active sites in metalloenzymes.[36] The extension of this structural motif to actinides presents a fortunate opportunity to compare the electronic structural interactions between transition elements, where both d- and f-orbitals are expected to contribute to covalent bonding.

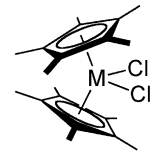

M = Ti, Zr, Hf, Th, U, Np

Of the approaches to experimentally measure covalent metal−ligand bonding interactions, ligand K-edge X-ray absorption spectroscopy (XAS) has been developed into a powerful technique to quantify ligand and metal orbital mixing in transition-metal bioinorganic and inorganic compounds.[37−49] This technique probes bound state transitions that occur on the low-energy side of the ligand K-edge and involves excitation of ligand 1s electrons into vacant molecular orbitals of primarily metal character[42] that also contain some ligand p character, due to covalent mixing. The integrated intensity of the pre-edge transition is a direct measure of the ligand p-orbital contribution to the primarily metal-based antibonding orbital. Hence, ligand K-edge XAS provides a direct experimental measure of covalency in metal−ligand bonding.[42]

The goal of this study is to establish that Cl K-edge XAS in combination with modern density functional theory (DFT) simulations can be used to probe the electronic structure, bonding, and covalency in light actinide (5f/6d) compounds for direct comparison with their 5d, 4d, and 3d counterparts. Given that **1**−**5** and $(C_5H_5)_2MCl_2$ (M = Ti, Zr, Hf, Th, U, **6**−**10**, respectively) have been the center of recent theoretical[15,50−61]

(10) Prodan, I. D.; Scuseria, G. E.; Martin, R. L. *Phys. Rev. B.* **2007**, *76*, 033101.
(11) Roger, M.; Belkhiri, L.; Arliguie, T.; Thuéry, P.; Boucekkine, A.; Ephritikhine, M. *Organometallics* **2008**, *27*, 33.
(12) Ingram, K. I. M.; Tassell, M. J.; Gaunt, A. J.; Kaltsoyannis, N. *Inorg. Chem.* **2008**, *47*, 7824.
(13) Gaunt, A. J.; Reilly, S. D.; Enriquez, A. E.; Scott, B. L.; Ibers, J. A.; Sekar, P.; Ingram, K. I. M.; Kaltsoyannis, N.; Neu, M. P. *Inorg. Chem.* **2008**, *47*, 29.
(14) Beach, D. B.; Bomben, K. D.; Edelstein, N. M.; Eisenberg, D. C.; Jolly, W. L.; Shinomoto, R.; Streitwieser, A., Jr. *Inorg. Chem.* **1986**, *25*, 1735.
(15) Bursten, B. E.; Strittmatter, R. J. *Angew. Chem., Int. Ed. Engl.* **1991**, *30*, 1069.
(16) Denning, R. G.; Green, J. C.; Hutchings, T. E.; Dallera, C.; Tagliaferri, A.; Giarda, K.; Brookes, N. B.; Braicovich, L. *J. Chem. Phys.* **2002**, *117*, 8008.
(17) O'Grady, E.; Kaltsoyannis, N. *J. Chem. Soc., Dalton Trans.* **2002**, 1233.
(18) Bercaw, J. E.; Marvich, R. H.; Bell, L. G.; Brintzinger, H. H. *J. Am. Chem. Soc.* **1972**, *94*, 1219.
(19) Manriquez, J. M.; McAlister, D. R.; Rosenberg, E.; Shiller, A. M.; Williamson, K. L.; Chan, S. I.; Bercaw, J. E. *J. Am. Chem. Soc.* **1978**, *100*, 3078.
(20) Roddick, D. M.; Fryzuk, M. D.; Seidler, P. F.; Hillhouse, G. L.; Bercaw, J. E. *Organometallics* **1985**, *4*, 97.
(21) Manriquez, J. M.; Fagan, P. J.; Marks, T. J.; Vollmer, S. H.; Day, C. S.; Day, V. W. *J. Am. Chem. Soc.* **1979**, *101*, 5075.
(22) Fagan, P. J.; Manriquez, J. M.; Maatta, E. A.; Seyam, A. M.; Marks, T. J. *J. Am. Chem. Soc.* **1981**, *103*, 6650.
(23) Kanellakopulos, B.; Aderhold, C.; Dornberger, E. *J. Organomet. Chem.* **1974**, *66*, 447.
(24) Ernst, R. D.; Kennelly, W. J.; Day, C. S.; Day, V. W.; Marks, T. J. *J. Am. Chem. Soc.* **1979**, *101*, 2656.
(25) Marks, T. J. *Prog. Inorg. Chem.* **1979**, *25*, 223.
(26) Marks, T. J.; Ernst, R. D. In *Comprehensive Organometallic Chemistry*; Wilkinson, G., Stone, F. G. A., Abel, E. W., Eds.; Pergamon: Oxford, U.K, 1982; Chapter 21, p 211.
(27) Edelmann, F. T. In *Comprehensive Organometallic Chemistry II*; Wilkinson, G., Stone, F. G. A., Abel, E. W., Eds.; Pergamon: Oxford, U.K., 1995; Chapter 2, p 131.
(28) Alt, H. G.; Koppl, A. *Chem. Rev.* **2000**, *100*, 1205.
(29) Möhring, P. C.; Coville, N. J. *Coord. Chem. Rev.* **2006**, *250*, 18.
(30) Evans, W. J.; Kozimor, S. A. *Coord. Chem. Rev.* **2006**, *250*, 911.
(31) Janiak, C. *Coord. Chem. Rev.* **2006**, *250*, 66.
(32) Herbert, D. E.; Mayer, U. F. J.; Manners, I. *Angew. Chem., Int. Ed.* **2007**, *46*, 5060.
(33) Gansauer, A.; Bluhm, H. *Chem. Rev.* **2000**, *100*, 2771.
(34) Parrish, J. D.; Shelton, D. R.; Little, R. D. *Org. Lett.* **2003**, *5*, 3615.
(35) Köpf-Maier, P.; Köpf, H. *Chem. Rev.* **1987**, *87*, 1137.
(36) Dombrowski, K. E.; Baldwin, W.; Sheats, J. E. *J. Organomet. Chem.* **1986**, *302*, 281.
(37) Hedman, B.; Hodgson, K. O.; Solomon, E. I. *J. Am. Chem. Soc.* **1990**, *112*, 1643.
(38) Shadle, S. E.; Hedman, B.; Hodgson, K. O.; Solomon, E. I. *Inorg. Chem.* **1994**, *33*, 4235.
(39) Shadle, S. E.; Hedman, B.; Hodgson, K. O.; Solomon, E. I. *J. Am. Chem. Soc.* **1995**, *117*, 2259.
(40) Glaser, T.; Hedman, B.; Hodgson, K. O.; Solomon, E. I. *Acc. Chem. Res.* **2000**, *33*, 859.
(41) Szilagyi, R. K.; Bryngelson, P. A.; Maroney, M. J.; Hedman, B.; Hodgson, K. O.; Solomon, E. I. *J. Am. Chem. Soc.* **2004**, *126*, 3018.
(42) Solomon, E. I.; Hedman, B.; Hodgson, K. O.; Dey, A.; Szilagyi, R. K. *Coord. Chem. Rev.* **2005**, *249*, 97.
(43) DeBeer George, S.; Brant, P.; Solomon, E. I. *J. Am. Chem. Soc.* **2005**, *127*, 667.
(44) DeBeer George, S.; Huang, K.-W.; Waymouth, R. M.; Solomon, E. I. *Inorg. Chem.* **2006**, *45*, 4468.
(45) Delgado-Jaime, M. U.; Conrad, J. C.; Fogg, D. E.; Kennepohl, P. *Inorg. Chim. Acta* **2006**, *359*, 3042.
(46) Ray, K.; DeBeer George, S.; Solomon, E. I.; Wieghardt, K.; Neese, F. *Chem.−Eur. J.* **2007**, *13*, 2783.
(47) Kozimor, S. A.; Yang, P.; Batista, E. R.; Boland, K. S.; Burns, C. J.; Christensen, C. N.; Clark, D. L.; Conradson, S. D.; Hay, P. J.; Lezama, J. S.; Martin, R. L.; Schwarz, D. E.; Wilkerson, M. P.; Wolfsberg, L. E. *Inorg. Chem.* **2008**, *47*, 5365.
(48) Harkins, S. B.; Mankad, N. P.; Miller, A. J. M.; Szilagyi, R. K.; Peters, J. C. *J. Am. Chem. Soc.* **2008**, *130*, 3478.
(49) Adhikari, D.; Mossin, S.; Basuli, F.; Huffman, J. C.; Szilagyi, R. K.; Meyer, K.; Mindiola, D. J. *J. Am. Chem. Soc.* **2008**, *130*, 3676.
(50) Petersen, J. L.; Lichtenberger, D. L.; Fenske, R. F.; Dahl, L. R. *J. Am. Chem. Soc.* **1975**, *97*, 6433.
(51) Lauher, J. W.; Hoffmann, R. *J. Am. Chem. Soc.* **1976**, *98*, 1729.
(52) Bursten, B. E.; Fang, A. *J. Am. Chem. Soc.* **1983**, *105*, 6495.
(53) Bruce, M. R. M.; Kenter, A.; Tyler, D. R. *J. Am. Chem. Soc.* **1984**, *106*, 639.
(54) Tatsumi, K.; Nakamura, A.; Hofmann, P.; Stauffert, P.; Hoffmann, R. *J. Am. Chem. Soc.* **1985**, *107*, 4440.
(55) Bursten, B. E.; Fang, A. *Inorg. Chim. Acta* **1985**, *110*, 153.
(56) Tatsumi, K.; Nakamura, A. *J. Am. Chem. Soc.* **1987**, *109*, 3195.
(57) Pepper, M.; Bursten, B. E. *Chem. Rev.* **1991**, *91*, 719.
(58) Green, J. C. *Chem. Soc. Rev.* **1998**, *27*, 263.
(59) Zachmanoglou, C. E.; Docrat, A.; Bridgewater, B. M.; Parkin, G.; Brandow, C. G.; Bercaw, J. E.; Jardine, C. N.; Lyall, M.; Green, J. C.; Keister, J. B. *J. Am. Chem. Soc.* **2002**, *124*, 9525.

and experimental[43,47,62−65] studies, they are well suited for a comparative Cl K-edge XAS study.

Experimental Section

General Considerations. All compounds and samples were manipulated under helium or nitrogen atmospheres with rigorous exclusion of air and moisture by Schlenk, glovebox, and glovebag techniques. Toluene was distilled over sodium and benzophenone and degassed by three freeze−pump−thaw cycles. Polystyrene was acquired from PolySciences Inc. as 3.0 μm dry form, exposed to a vacuum (10^{-3} Torr) for 24 h before use, and verified to contain no chlorine by Cl K-edge XAS. The D_{2d} Cs_2CuCl_4 intensity and energy calibration standard[39,42,66−69] was prepared as previously described.[70] The $(C_5Me_5)_2MCl_2$ (M = Ti, **1**;[18] Zr,[19] **2**; Hf,[20] **3**) compounds were obtained from Aldrich and crystallized from saturated solutions of hot toluene that were slowly cooled to −25 °C. The $(C_5Me_5)_2AnCl_2$ (An = Th,[21,22] **4**; U,[21,22] **5**) compounds were synthesized as previously described and purified by crystallization from saturated solutions of hot toluene that were slowly cooled to −25 °C. The sample purity for all compounds was confirmed by ^{1}H NMR spectroscopy.[18−22]

XAS Sample Preparation. Samples were prepared by finely grinding the analyte (0.007 g) with 3 μm polystyrene beads (0.120 g) to obtain a homogeneous mixture that contained, by mass, 5.5% analyte as described previously.[47] An aliquot of this mixture (0.010 g) was transferred to a vial that contained polystyrene beads (0.070 g), and this new diluted mixture, which contained 0.69% analyte by mass, was ground with a mortar and pestle for 2 min to achieve small and finely divided particles. An aliquot of this mixture (0.060 g) was transferred to a vial, and toluene (400 μL) was added. The mixture was stirred with a glass stir rod until everything dissolved, and the resulting solution was transferred into a 5 × 11 × 4 mm well that had been bored into an aluminum block. The toluene was allowed to evaporate for 48 h under the helium atmosphere of the glovebox, leaving a robust film fixed within the sample block. This approach is important for two reasons. First, the polystyrene gives a suitable matrix for encapsulating radioactive materials (Th, U), and the analytical procedure gives high reproducibility for sample preparation, which has been shown to eliminate self-absorption effects in Cl XAS.[47]

Chlorine K-Edge XAS Measurements. The room temperature Cl XAS data were recorded at the Stanford Synchrotron Radiation Laboratory (SSRL) and analyzed using the 54-pole wiggler beamline 6-2 under ring conditions of 3.0 GeV and 85−100 mA in a high magnetic field mode of 0.9 T with a Ni-coated harmonic rejection mirror and a fully tuned (3150 eV) Si(111) double-crystal monochromator. A chamber similar to that previously described was used,[69] with the exception that two additional layers of radiological containment were introduced, first with a beryllium window (50 μm thick) to separate the I_0 chamber from the beam pipe, followed by a 4.5 μm polypropylene window to separate the I_0 and I_1 chambers. The sample excitation fluorescence was measured under vacuum (10^{-9} Torr), and the Cl K-edge XAS spectrum was collected against the incident beam using pairs of backward-facing International Radiation Detector XUV100 type photodiodes coated with 1000 Å of Al. The photodiodes were closely spaced so that a 1−2 mm wide beam passed between them. The incident beam intensity was measured as the scatter off of the He atmosphere with a photodiode pair in a front chamber. Fluorescence from the sample was measured by an identically configured photodiode pair facing the sample that was mounted at normal incidence to the oncoming beam that collected over a wide solid angle because of its 5−10 mm proximity to the sample. The energy calibrations for Cl K-edge XAS were repeatedly conducted between sample scans and based on the maximum of the first pre-edge feature in the Cl K-edge XAS of D_{2d} Cs_2CuCl_4[39,42,66−70] at 2820.20 eV.

The Cl K-edge XAS data were collected with three different step sizes, which were 4.000, 0.072, and 3.899 eV for the pre-edge (2705−2801 eV), edge (2801−2835 eV), and postedge (2835−3140 eV) regions, respectively. To obtain adequate statistics, 4 s counting times were employed and the spectra were collected twice. Different samples of crystalline **1**−**5** were examined during three different synchrotron runs to confirm reproducibility and establish error limits with the measurements. Error limits associated with the intensities for the resolved pre-edge features for **2**, **3**, and **5** are 1%, while a larger margin of error is associated with the greater variability associated with reproducing the intensities of the pre-edge features of **1** and the poorly resolved pre-edge shoulder in the Cl K-edge XAS of **4**.

XAS Data Analysis. Data manipulation and analyses were similar to those described by Solomon and co-workers.[42] For example, in typical data analysis for Cl K-edge XAS, a first-order polynomial was fit to the pre-edge region (2780.0−2817.0 eV) and then subtracted from the experimental data to eliminate the background of the spectrum. The data were normalized by fitting a first-order polynomial to the postedge region of the spectrum (2830.0−3032.0 eV) and by setting the edge jump at 2835.0 eV to an intensity of 1.0.[42] This normalization procedure gives spectra normalized to a single Cl atom or M−Cl bond. Curve-fitting analyses were conducted using the mathematical expressions for Voigt and step functions employed by EDG_FIT[71] in a manner identical to that described by Solomon and co-workers.[42] For convenience, we have utilized these expressions in the program IGOR 6.0. Curve fits were performed over several energy ranges. The first and second derivatives of each spectrum were used as guides to determine the number and positions of the spectral features for the curve-fitting analyses. Curve fits utilized pseudo-Voigt line shapes and a step function to model the pre-edge and rising edge spectral features.[42] For the pre-edge and white line features, a fixed 1:1 ratio of Lorentzian to Gaussian contributions was used, and for the step function, a 1:1 ratio of arctangent and error function contributions was employed.[42] The area under the pre-edge peaks (hereafter defined as the intensity) was compared to that of the well-established Cl K-edge intensity standard Cs_2CuCl_4. Solomon and co-workers report this feature to have a normalized pre-edge intensity of 0.53 corresponding to 7.5% Cl 3p character.[42] Using our polystyrene encapsulation methodology, we routinely reproduce these pre-edge intensities between 0.50 and 0.55. We take this as evidence that we can determine the amount of Cl 3p character to ±1%.

Electronic Structure Calculations. Electronic structure calculations were conducted on the $(C_5Me_5)_2MCl_2$ (M = Ti, Zr, Hf, Th, U, **1**−**5**, respectively) and $(C_5H_5)_2AnCl_2$ (An = Th, **9**; U, **10**) complexes using B3LYP hybrid DFT[72] in the Gaussian 03 code.[73] The Stuttgart 97 relativistic effective core potential (RECP) and

(60) Wang, X.; Chen, L.; Endou, A.; Kubo, M.; Miyamoto, A. *J. Organomet. Chem.* **2003**, *678*, 156.
(61) Casarin, M.; Finetti, P.; Vittadini, A.; Wang, F.; Ziegler, T. *J. Phys. Chem. A* **2007**, *111*, 5270.
(62) Condorelli, G.; Fragalá, I.; Centineo, A.; Tondello, E. *J. Organomet. Chem.* **1975**, *87*, 311.
(63) Fragalá, I.; Marks, T. J.; Fagan, P. J.; Manriquez, J. M. *J. Electron Spectrosc. Relat. Phenom.* **1980**, *20*, 249.
(64) Ciliberto, E.; Condorelli, G.; Fagan, P. J.; Manriquez, J. M.; Fragalá, I.; Marks, T. J. *J. Am. Chem. Soc.* **1981**, *103*, 4755.
(65) King, W. A.; Di Bella, S.; Gulino, A.; Lanza, G.; Fragalá, I. L.; Stern, C. L.; Marks, T. J. *J. Am. Chem. Soc.* **1999**, *121*, 355.
(66) Gewirth, A. A.; Cohen, S. L.; Schugar, H. J.; Solomon, E. I. *Inorg. Chem.* **1987**, *26*, 1133.
(67) Didziulis, S. V.; Cohen, S. L.; Gewirth, A. A.; Solomon, E. I. *J. Am. Chem. Soc.* **1988**, *110*, 250.
(68) Neese, F.; Hedman, B.; Hodgson, K. O.; Solomon, E. I. *Inorg. Chem.* **1999**, *38*, 4854.
(69) Shadle, S. E. Ph.D. Thesis, Stanford University, 1994.
(70) Helmholz, L.; Kruh, R. F. *J. Am. Chem. Soc.* **1952**, *74*, 1176.
(71) George, G. N. *EDG_FIT*; Stanford Synchrotron Radiation Laboratory, Stanford Linear Accelerator Center, Stanford University: Stanford, CA.

associated basis sets (minus the most diffuse function) were used for Ti, Zr, Hf, Th, and U. For the C and H atoms the 6-31G* basis set was used, while for Cl the 6-31G* basis set was modified by recontracting the p functions to the B3LYP 2p through 6p atomic orbitals of Cl^- (see the Supporting Information). The recontraction of the p space did not change the predicted structures and proved advantageous by providing a cleaner interpretation of the participating atomic orbitals in the molecular orbitals under consideration. These functionals and basis sets have been extensively tested for organometallic systems and shown to give good agreement with experimental data.[74−79] The populations of the Cl 3p orbitals of each compound were then obtained by Mulliken population analysis of each particular molecular orbital.

Simulated Cl K-Edge Spectra. For closed-shell molecules of formulas $(C_5Me_5)_2MCl_2$ (M = Ti, Zr, Hf, Th, **1**−**4**, respectively) and $(C_5H_5)_2ThCl_2$, **9**, Cl K-edge XAS were simulated using time-dependent density functional theory (TD-DFT). This approach involves evaluating core electron excitations by exploiting the small amount of mixing of the core orbitals with the high-lying unoccupied virtual orbitals. Specifically this analysis involves a linear response calculation, which enables the probability amplitudes to be extracted from the transition densities and dipole moments between the calculated excited states and the ground states. The excitations originating from all of the intermediate states between the Cl 1s-orbital and the HOMO were "frozen"; that is, they were excluded so that only excitations from the core levels to virtual molecular orbitals could be analyzed. This allows the virtual orbitals to mix and reflect the presence of the core hole in chlorine. However, relaxations for the other occupied orbitals associated with the core hole are not included. Although excluding relaxations in the occupied orbitals associated with the core hole results in large errors associated with absolute calculated transition energies, this computation technique addresses the first-order changes in virtual orbitals accompanying the core hole excitation and has been shown to be in very good agreement with experimental measurements made on transition-metal compounds.[47] This was achieved by establishing an energy shift of 64.9 eV for all calculated transition-metal spectra to account for the omission of the atomic relaxation associated with the core excitation, relativistic stabilization, and errors associated with the functional.[80] Line broadening of ca. 1.0 eV was applied to emulate the experimental line widths. For actinide systems, this constant shift of 64.9 eV may not sufficiently account for the omission of the atomic and extra-atomic relaxation associated with the core excitation, relativistic stabilization, and errors associated with the functional.[80] Therefore, for comparison of calculated spectral transitions with experimental data for actinide systems, we chose to set the energy of the first 6d peak to be that of the experimentally determined peak. This resulted in an energy shift of 65.9 eV for the $(C_5Me_5)_2ThCl_2$ TD-DFT calculation and a 63.4 eV shift for the $(C_5Me_5)_2UCl_2$ transition dipole calculation.

TD-DFT is of questionable use for the description of molecules with open-shell ground states within the Gaussian 03 program. This is because excitations that involve a change in spin quantum number (i.e., from α to β spin) are not presently available in Gaussian 03. Therefore, in addition to TD-DFT we examined an approximation to the DFT linear response methodology that simply consists of calculating transition dipoles among ground-state molecular orbitals. Our approach to calculate transition dipoles from Gaussian 03 output is to use the dipole moment matrices among atomic orbital basis sets and the molecular orbital coefficient from the output file. With those two pieces of data it is straightforward to calculate transition dipole moments among molecular orbitals via a change of basis set as follows. If we indicate the ith atomic orbital basis function by $|\phi_i\rangle$, an arbitrary occupied orbital can be written as

$$|\psi^{\mathrm{occ}}\rangle = \sum_i a_i|\phi_i\rangle$$

where a_i is the ith expansion coefficient from the Gaussian 03 output. An arbitrary virtual orbital can be written as

$$|\psi^{\mathrm{vir}}\rangle = \sum_j b_j|\phi_j\rangle$$

The transition dipole moment from $|\psi^{\mathrm{occ}}\rangle$ to $|\psi^{\mathrm{vir}}\rangle$ can be obtained with the matrix product

$$\boldsymbol{\mu} = \langle\psi^{\mathrm{occ}}|\mathbf{r}|\psi^{\mathrm{vir}}\rangle = \sum_i \sum_j a_i^* b_j \langle\phi_i|\mathbf{r}|\phi_j\rangle$$

$$\boldsymbol{\mu}^{\mathrm{occ}\rightarrow\mathrm{vir}} = \sum_i \sum_j a_i^* b_j M_{ij}$$

where M_{ij} corresponds to the element (i, j) of the dipole matrix in atomic orbital basis functions and a_i and b_j are the coefficients of the molecular orbitals. This approach was tested against TD-DFT for the closed-shell ground-state species **1**−**4**. The spectra calculated from the MO transition dipoles are essentially identical to those from the TD-DFT calculations including the most salient features such as pre-edge features, the relative intensity of the peaks, and the position of the rising edge. With this validation of the transition dipole method on closed-shell systems **1**−**4**, we employed the transition dipole approach to simulate spectra for the open-shell $(C_5R_5)_2UCl_2$ (R = Me, **5**; H, **10**) systems. Note that our approach also ignores the final-state multiplet structure in the uranium electronic manifold. A more rigorous analysis for this open-shell system is under way which includes the four component relativistic effects, spin−orbital interactions, open-shell TD-DFT, and multiplet effects. All the calculated transition intensities were evenly broadened with a pseudo-Voigt function of half-width at half-maximum of 0.33 eV and equal amounts of Gaussian and Lorentzian functions to emulate, as close as possible, the experimental spectrum.

Results and Discussion

The background-subtracted and normalized chlorine K-edge XAS spectra for the $(C_5Me_5)_2MCl_2$ (M = Ti, Zr, Hf, Th, U, **1**−**5**, respectively) compounds are shown in Figure 1. Samples were encapsulated in polystyrene matrixes (0.7% by mass of analyte) as an approach for safe containment of radioactive materials with simultaneous minimization of X-ray self-absorption.[47] This also avoids the implementation of additional windows and chambers (radiological containment) that can attenuate the incident radiation and sample fluorescence.

The Cl K-edge XAS spectra for the transition-metal $(C_5Me_5)_2MCl_2$ (M = Ti, **1**; Zr, **2**; Hf, **3**) complexes are similar to the Cl K-edge XAS spectra reported for the hydrogen-substituted $(C_5H_5)_2MCl_2$ (M = Ti, Zr, Hf, **6**−**8**, respectively) analogues in that pre-edge features indicative of covalent M−Cl interactions are apparent between 2821 and 2824 eV, Figure 1 and Table 1.[43,47] For these compounds, the energy positions of

(72) Becke, A. D. *J. Chem. Phys.* **1993**, *98*, 5648.
(73) Frisch, M. J. *Gaussian 03*; Gaussian Inc.: Wallingford, CT, 2004.
(74) Kuchle, W.; Dolg, M.; Stoll, H.; Preuss, H. *J. Chem. Phys.* **1994**, *100*, 7535.
(75) Clark, A. E.; Martin, R. L.; Hay, P. J.; Green, J. C.; Jantunen, K. C.; Kiplinger, J. L. *J. Phys. Chem. A* **2005**, *109*, 5481.
(76) Bi, S.; Lin, Z.; Jordan, R. F. *Organometallics* **2004**, *23*, 4882.
(77) Hay, P. J. *Organometallics* **2007**, *26*, 4424.
(78) Karttunen, V. A.; Linnolahti, M.; Pakkanen, T. A.; Maaranen, J.; Pitkänen, P. *Theor. Chem. Acc.* **2007**, *118*, 899.
(79) Graves, C. R.; Yang, P.; Kozimor, S. A.; Vaughn, A. E.; Clark, D. L.; Conradson, S. D.; Schelter, E. J.; Scott, B. L.; Thompson, J. D.; Hay, P. J.; Morris, D. E.; Kiplinger, J. L. *J. Am. Chem. Soc.* **2008**, *130*, 5272.
(80) Martin, R. L.; Shirley, D. A. Many-electron theory of photoemission. *Electron Spectroscopy, Theory, Techniques and Applications*; Academic Press: New York, 1977; Vol. 1, p 75.

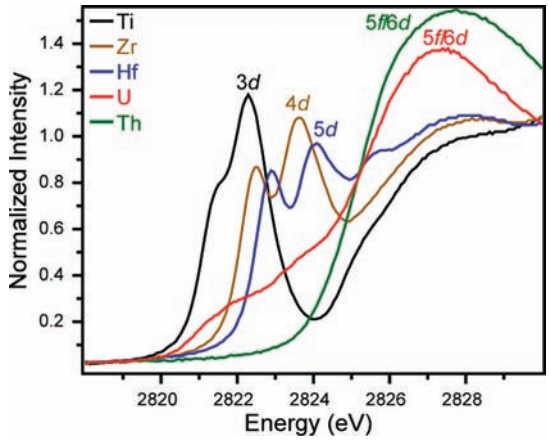

Figure 1. Experimental Cl K-edge X-ray absorption spectra for polystyrene-encapsulated samples of $(C_5Me_5)_2MCl_2$ (M = Ti (black), Zr (brown), Hf (blue), Th (green), U (red), **1**−**5**, respectively).

the pre-edge peaks are not largely affected by the identity of the ancillary ligand, i.e., $(C_5Me_5)^-$ vs $(C_5H_5)^-$, Table 1.

Significant pre-edge energy shifts occur when the metal ion is changed from 3d to 4d to 5d. For example, the pre-edge peaks for $(C_5Me_5)_2MCl_2$ (M = Ti, Zr, Hf) are well-resolved and increase in energy as we move from Ti to Zr and Hf, Table 1. This is consistent with trends observed for the $(C_5H_5)_2MCl_2$ analogues, which demonstrated that pre-edge peak energies increase with increasing principal quantum number,[47] such that Ti < Zr < Hf, and reflects the expected rise in energy for the 3d-, 4d-, and 5d-orbital final states. The actinide analogues **4** and **5** show markedly different Cl K-edge XAS spectra in comparison to the transition-metal systems **1**−**3**, Figure 1. For $(C_5Me_5)_2UCl_2$, **5**, there are three distinct pre-edge features, as confirmed by the second derivate analysis of the spectrum. For $(C_5Me_5)_2ThCl_2$, **4**, there are no pre-edge features by visible inspection, although the second and fourth derivatives suggest the presence of one shoulder close to the rising edge that could not be resolved.

Cl K-Edge XAS of Transition-Metal Complexes. Although the pre-edge features in the Cl K-edge XAS for **1**−**3** are well-resolved from the white lines, the close proximity of the pre-edge features in **2** and **3** to the rising edges complicates rigorous determination of inflection points for the white lines, Figure 1. The spectra for **1**−**3** also contain a shoulder on the rising edge that is more pronounced in the $(C_5Me_5)_2HfCl_2$ case than for $(C_5Me_5)_2TiCl_2$. This shoulder further complicates identification of the inflection points for rising edge determination.

The spectral features of **1**−**3** were modeled using pseudo-Voigt line shapes with a fixed 1:1 Lorentzian to Gaussian ratio, Figure 2.[42] For $(C_5Me_5)_2MCl_2$ (M = Ti, **1**; Zr, **2**), the curve-fitting analysis and the first and second derivatives of the data reveal that the pre-edge features are well modeled by two functions. Another gauge that can be used to assess the curve-fitting model relies on evaluating the shapes of residual peaks, which are obtained by subtracting from the data the functions used to generate the fit, with the exception of the function used to model the peak of interest. For **1** and **2**, the residual peaks are symmetric and similar in shape to the corresponding pseudo-Voigt functions. This indicates a good fit and suggests that the two pre-edge features can be resolved with confidence. This type of analysis is common for evaluating curve-fitting in EXAFS,[79,81,82] and we find it to be extremely useful in evaluating XAS spectra for covalency studies.

The Cl K-edge XAS of $(C_5Me_5)_2HfCl_2$, **3**, provides an example where employing residual data and residual peak shape analysis provided unique insight. For example, fitting the pre-edge region of the Cl K-edge XAS spectrum of **3** with two pre-edge features in analogy to $(C_5Me_5)_2ZrCl_2$, **2**, and $(C_5H_5)_2MCl_2$ (M = Ti, Zr, Hf, **6**−**8**, respectively) provided an adequate model with good correlation coefficients. However, the residual data deviated significantly from zero near 2824 eV, and the residual pre-edge and postedge peaks were highly asymmetric. This prompted closer analysis of the first and second derivatives, which suggested that a third feature had been missed and should be considered for analysis of the Cl K-edge XAS spectrum of **3**, Figure 2. Including this third pre-edge feature in the curve fit did improve the correlation coefficient. Moreover, with three features, the residual data do not appreciably deviate from zero and the three resulting highly symmetric pre-edge and postedge residual peaks (see the Supporting Information) are similar in shape to the pseudo-Voigt functions used to generate the fit. The presence of this third feature does not appreciably affect the peak positions of the first two features or the total pre-edge peak intensities. It does, however, represent a slight difference between the electronic structure model of $(C_5Me_5)_2HfCl_2$ relative to **1** and **2** and to the $(C_5H_5)_2MCl_2$ analogues, vide infra. Hence, the Cl K-edge XAS spectrum of $(C_5Me_5)_2HfCl_2$ demonstrates a limitation associated with relying too heavily on correlation coefficients alone for evaluating modeled data and suggests that residual data and residual peak analysis can provide useful insights and additional confidence for interpreting Cl K-edge XAS spectra.

The amount of Cl 3p character (%) in virtual d-orbitals was determined for **1**−**3** using the pre-edge intensities derived from curve fits (pseudo-Voigt functions) and compared to the well-established pre-edge peak intensity of D_{2d} Cs_2CuCl_4 that contains 7.5% Cl 3p character per M−Cl bond,[39,42,66−70] Table 1. The two pre-edge peak intensities of 0.30 and 1.48 for $(C_5Me_5)_2TiCl_2$, **1**, and 0.51 and 1.08 for $(C_5Me_5)_2ZrCl_2$, **2**, correspond to a total of 25% and 23% Cl 3p character per M−Cl bond for **1** and **2**, respectively. For $(C_5Me_5)_2HfCl_2$, **3**, the three pre-edge peak intensities of 0.62, 0.56, and 0.35 correspond to 22% Cl 3p character for each Hf−Cl bond. Although the magnitudes of the total Cl 3p contributions to the virtual d-orbitals (25%, 23%, and 22%) in $(C_5Me_5)_2MCl_2$ compounds decrease, such that Ti > Zr > Hf, given the experimental error of ∼1%, these values are essentially indistinguishable within 3σ, Table 2. This is similar to what was previously reported for the analogous $(C_5H_5)_2MCl_2$ (M = Ti, Zr, Hf, **6**−**8**, respectively) compounds.[42]

Cl K-Edge XAS of Actinide Complexes. From visual inspection, the Cl K-edge XAS spectrum for $(C_5Me_5)_2ThCl_2$, **4**, differs from those of the transition-metal analogues in that it does not appear to contain any pre-edge features. Examination of the second- and fourth-derivative spectra, Figure 3, indicates the presence of a weak shoulder above 2824 eV, which is in agreement with expectations from electronic structure calculations, vide infra. For curve-fitting of the data, there are a number of models that fit the postedge region, resulting in significant

(81) Clark, D. L.; Conradson, S. D.; Donohoe, R. J.; Keogh, D. W.; Morris, D. E.; Palmer, P. D.; Rogers, R. D.; Tait, C. D. *Inorg. Chem.* **1999**, *38*, 1456.
(82) Conradson, S. D.; Manara, D.; Wastin, F.; Clark, D. L.; Lander, G. H.; Morales, L. A.; Rebizant, J.; Rondinella, V. V. *Inorg. Chem.* **2004**, *43*, 6922.

Table 1. Comparison of Experimental and Calculated Pre-Edge Peak Energies (eV), Intensities, and Amounts of Cl 3p Character[a] (%) for the Polystyrene-Encapsulated $(C_5Me_5)_2MCl_2$ Complexes (M = Ti, Zr, Hf, Th, U, **1**−**5**, Respectively)

	peak 1				peak 2				peak 3			
			amt of Cl 3p character				amt of Cl 3p character				amt of Cl 3p character	
compd	energy(exptl)	intensity(exptl)	exptl	calcd	energy(exptl)	intensity(exptl)	exptl	calcd	energy(exptl)	intensity(exptl)	exptl	calcd
$D_{2d}Cs_2CuCl_4$[42]	2820.20	0.53	7.5	7.5								
$(C_5Me_5)_2TiCl_2$, **1**	2821.31	0.30	4.3	4.9	2822.31	1.48	20.9	11.0				
$(C_5Me_5)_2ZrCl_2$, **2**	2822.41	0.51	7.2	4.9	2823.62	1.08	15.3	9.0				
$(C_5Me_5)_2HfCl_2$, **3**	2822.86	0.62	8.8	4.7	2823.93	0.56	7.9	2.8	2824.56	0.35	5.0	4.4
$(C_5Me_5)_2ThCl_2$, **4**				8.9								
$(C_5Me_5)_2UCl_2$, **5**	2821.17	0.05	0.7	2.9	2821.99	0.19	2.7	5.0	2823.44	0.40	5.7	3.7

[a] The amount of Cl 3p character is reported per M−Cl bond.

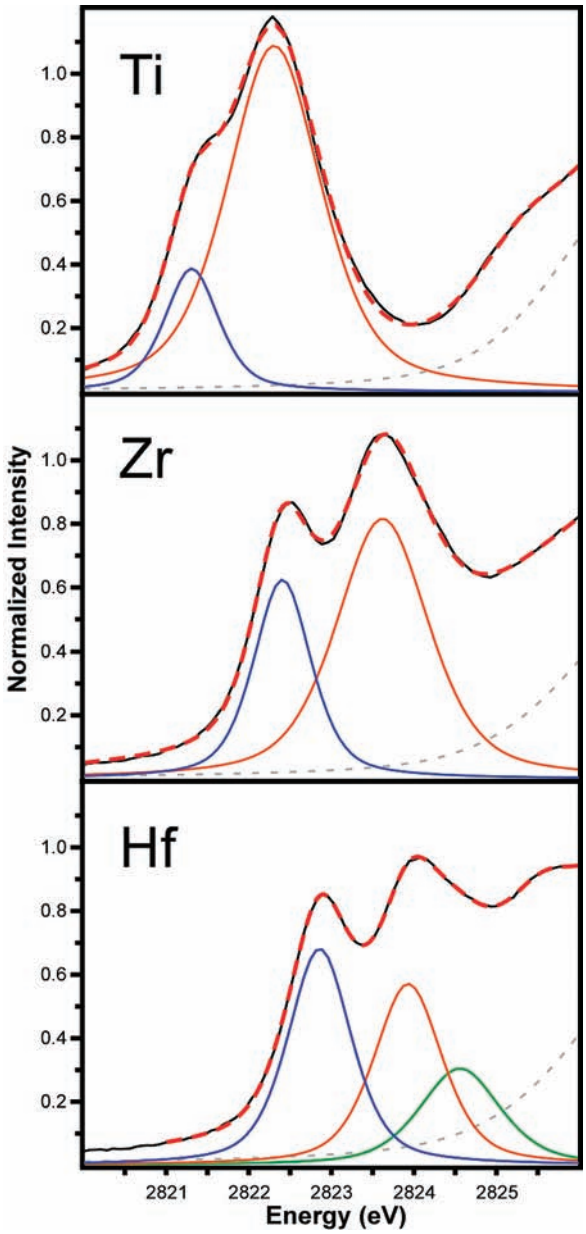

Figure 2. Cl K-edge X-ray absorption spectra (black line), curve fits (red dashed line), pre-edge pseudo-Voigt peaks (blue, orange, and green lines), and the rising edge of a postedge pseudo-Voigt peak used to generate the fit (gray dashed line) for polystyrene film samples of $(C_5Me_5)_2MCl_2$ (M = Ti (top), Zr (center), Hf (bottom), **1**−**3**, respectively).

variation in the fitted pre-edge peak intensity. The resulting uncertainty in the peak area is therefore high, and we conclude

Table 2. Comparison of Experimental and Calculated Total Pre-Edge Peak Intensities and Total Amounts of Cl 3p Character[a] (%) for the Polystyrene-Encapsulated $(C_5R_5)_2MCl_2$ Complexes (M = Ti, Zr, Hf, Th, U; R = H, Me)

		total amt of Cl 3p character	
compd	intensity(exptl)	exptl	calcd
$D_{2d}Cs_2CuCl_4$[42]	0.53	7.5	
$(C_5Me_5)_2TiCl_2$, **1**	1.78	25	16
$(C_5Me_5)_2ZrCl_2$, **2**	1.59	23	14
$(C_5Me_5)_2HfCl_2$, **3**	1.53	22	12
$(C_5Me_5)_2ThCl_2$, **4**			9
$(C_5Me_5)_2UCl_2$, **5**	0.64	9	12
$(C_5H_5)_2TiCl_2$, **6**[b]	1.81	25	20
$(C_5H_5)_2ZrCl_2$, **7**[47]	1.78	25	18
$(C_5H_5)_2HfCl_2$, **8**[47]	1.34	19	17
$(C_5H_5)_2ThCl_2$, **9**			17
$(C_5H_5)_2UCl_2$, **10**			16

[a] The amount of Cl 3p character is reported per M−Cl bond. [b] Although compound **6** has been the focus of previous experimental and theoretical investigations,[43,47,61] the experimental values in this table are from previous analyses made on samples that had been encapsulated in polystyrene.[47] The calculated values were conducted in a fashion similar to that for compounds **1**−**4**.[47]

that the pre-edge shoulder for **4** is not sufficiently resolved to extract meaningful experimental intensities.

In contrast to $(C_5Me_5)_2ThCl_2$, **4**, the Cl K-edge XAS spectrum for $(C_5Me_5)_2UCl_2$, **5**, contains three clear pre-edge features that can be resolved from the rising edge, Figure 3. These features were also modeled using pseudo-Voigt line shapes with a fixed 1:1 Lorentzian to Gaussian ratio, Figure 3. The correlation coefficients, residual data, and residual peak shapes suggest that the curve-fitting analysis provides a good model for the experimental data. From the curve fits, we find that the first two peaks at 2821.17 and 2821.99 eV in the Cl K- edge XAS spectrum of $(C_5Me_5)_2UCl_2$, **5**, are similar in energy to the first peak observed for $(C_5Me_5)_2TiCl_2$ (2821.31 eV), which was assigned to a transition into a 3d-orbital, Table 1. The third peak for **5** at 2823.44 eV is higher in energy than the first peak observed for $(C_5Me_5)_2HfCl_2$ (2822.86 eV), which was assigned to a transition into a 5d-orbital. Considerations of the increase in energy observed for transitions into 3d-, 4d-, and 5d-orbitals for Ti, Zr, and Hf (respectively) lead to the expectation that a transition into a 6d-orbital will be slightly higher in energy than that into a 5d-orbital. Hence, the third pre-edge peak in the U analogue is reasonably assigned to a Cl 1s transition into U 6d-orbitals, leaving the two lower energy peaks as potential transitions into 5f-orbitals.

The pre-edge intensities for $(C_5Me_5)_2UCl_2$, **5**, derived from pseudo-Voigt functions are 0.05, 0.19, and 0.40 for a total intensity of 0.64. Relative to the D_{2d} Cs_2CuCl_4 intensity standard,[39,42,66−70] this total intensity corresponds to 9% Cl 3p character per U−Cl bond. This value is approximately half of

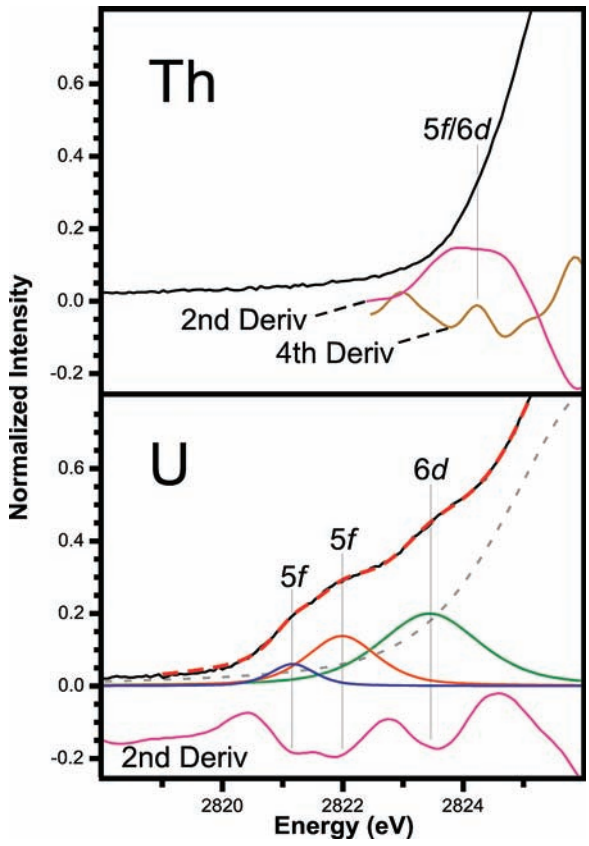

Figure 3. (Top) Cl K-edge X-ray absorption spectrum (black line) and second (purple line) and fourth (brown line) derivative spectra for $(C_5Me_5)_2ThCl_2$, **4**, indicating the presence of a pre-edge shoulder in **4**. (Bottom) Cl K-edge X-ray absorption spectrum (black line), curve fit (red dashed line), second-derivative spectrum (purple line), the pre-edge pseudo-Voigt peaks (blue, orange, and green lines), a postedge pseudo-Voigt peak (gray dashed line) used to generate the fits for $(C_5Me_5)_2UCl_2$, **5**.

the Cl 3p mixing that was observed in the analogous group IV transition-metal counterparts, which ranged from 22% to 25%, Tables 1 and 2. Given that covalency in 5f-element chemistry has been highly debated for decades, this is a significant finding.[3−17] The Cl K-edge XAS spectrum of **5** shows direct experimental evidence for covalency in metal-ligand bonding and provides a quantitative assessment of the degree of orbital mixing between U and Cl in the U−Cl bonds of **5**. For better guidance in peak assignments, and assessment of the relative roles of 5f- versus 6d-orbitals in bonding, we turn to electronic structure calculations.

Ground-State Electronic Structure Calculations. DFT calculations on $(C_5Me_5)_2MCl_2$ (M = Ti, **1**; Zr, **2**; Hf, **3**) indicate that the electronic structures of **1**−**3** are quite similar to those of their $(C_5H_5)_2MCl_2$ analogues,[43,47,61] and Table 3 reports the α orbital energies. The β orbital energies are nearly identical, the largest differences being on the order of 0.2 eV. The calculations show that the HOMO and the subsequent three lower lying orbitals have predominantly C_5Me_5 character with only a small contribution from the M−Cl bonds. These occupied orbitals are approximately 1 eV higher in energy than a block of six primarily Cl 3p-orbitals that span only ∼1.2 eV. For **1**−**3**, the first five unoccupied orbitals have predominantly metal *n*d character with a calculated HOMO/LUMO gap of 3.58, 4.22, and 4.51 eV for **1**, **2**, and **3**, respectively. For all three transition-metal $(C_5Me_5)_2MCl_2$ complexes, the LUMO has $1a_1$ symmetry and is best described as M−Cl π-antibonding. This orbital is significantly lower in energy than a higher lying set of four primarily metal *n*d molecular orbitals ($1b_2$, $1b_1$, $1a_2$, and $2a_1$), which are M−Cl σ-, π-, π-, and σ-antibonding, respectively. For Ti and Zr (**1**, **2**), these four *n*d-orbitals span only ca. 0.9 eV, Figure 4, resulting in a d-orbital energy pattern similar to that reported for $(C_5H_5)_2MCl_2$ (M = Ti, Zr, Hf).[43,47,61] In contrast, for $(C_5Me_5)_2HfCl_2$, **3**, we find a low-lying $1a_1$ orbital, an intermediate $1b_2$ orbital, and a manifold of three higher lying orbitals of $1b_1$, $1a_2$, and $2a_1$ symmetries, Figure 4. It has previously been shown that all five *n*d-orbitals are necessary to understand the XAS intensities due to a combination of σ and π orbital interactions with the Cl levels at lower energy.[43,47,61] The resulting d-orbital splitting pattern will be important for the interpretation of the XAS spectrum of **3**.

The DFT calculations conducted on the optimized structures of $(C_5R_5)_2AnCl_2$ (An = Th, U; R = H, Me) show that the actinide complexes contain many similarities to their transition-metal analogues. These calculations show that the bonding orbitals for both $(C_5Me_5)_2UCl_2$, **5**, and $(C_5H_5)_2UCl_2$, **10**, can be described as having four occupied predominantly cyclopentadienyl orbitals above six occupied orbitals that have mainly Cl 3p character, which is analogous to what was observed in **1**−**3** and **6**−**9**.[43,47,61] The open-shell calculations for the hydrogen-substituted $(C_5H_5)_2UCl_2$ complex indicate that the two highest lying occupied molecular orbitals have predominantly 5f character, giving the expected f^2 triplet-ground-state configuration for U(IV), and are close in energy to other occupied cyclopentadienyl orbitals; see the Supporting Information. This general ordering of occupied Cl and C_5H_5 orbitals followed by 5f-orbitals is similar to Xα-SW calculations previously reported for $(C_5H_5)_2UCl_2$,[52] **10**, where the 5f electrons were artificially spin paired to run the calculation. In contrast, for $(C_5Me_5)_2UCl_2$, **5**, the highest two α spin orbitals are mainly C_5Me_5 based but have matches found in the β spin orbitals and hence do not represent unpaired spin density. The orbitals containing the unpaired spin lie lower in energy and are again dominated by U 5f character. This is confirmed by a natural orbital analysis, which generates two largely U 5f-orbitals with an occupation number close to 1; see the Supporting Information. For both **5** and **10**, there are approximately 3 eV differences between the occupied and unoccupied 5f-orbitals, Figure 4 and Table 4. However, caution must be exercised when interpreting these ground-state DFT orbital energies for open-shell systems to explain the peak splitting observed in experiments without including spin−orbit interactions and multiplet effects.

For $(C_5Me_5)_2UCl_2$, **5**, and $(C_5H_5)_2UCl_2$, **10**, we find a group of five virtual 6d-orbitals that are nearly identical to those found in the transition-metal systems, as shown for **5** in Figure 4. Superimposed on this 6d-orbital picture, and at lower energy, is the addition of the 5f-orbital manifold, which has a combination of σ- and π-antibonding interactions with the Cl lone pairs. For **5**, steric repulsion between the two C_5Me_5 rings gave an optimized geometry with C_1 symmetry, which complicates the bonding comparison to the transition-metal analogues. To better facilitate a comparison to transition elements, calculations were performed on $(C_5H_5)_2UCl_2$, **10**, in both the geometry-optimized C_1 symmetry and in rigorous C_{2v} symmetry. Both calculations provide bonding descriptions similar to that observed for $(C_5Me_5)_2UCl_2$ in C_1 symmetry, Table 4, but the results for C_{2v} symmetry reduce the amount of orbital mixing between orbitals of identical symmetry and make it easier to describe the bonding interactions to a broad readership. The calculated Kohn−Sham orbitals for **10** constrained to C_{2v} symmetry are shown in Figure

Table 3. Orbital Composition (%) for the Five Primarily Metal d-Based Orbitals Showing the Calculated Total Amount of Cl 3p Character (%) for the Specified Orbitals in $(C_5Me_5)_2MCl_2$ (M = Ti, Zr, Hf)[a]

	MO label (symmetry)					
	59 ($1a_1$) (LUMO)	60 ($1b_2$)	61 ($1b_1$)	62 ($1a_2$)	63 ($2a_1$)	total amt of Cl 3p character (59−63)
			$(C_5Me_5)_2TiCl_2$, **1**			
energy (eV)	−2.14	−1.29	−1.17	−1.04	−0.86	
total amt of Ti 3d character	79.4	57.2	70.4	68.4	72	
total amt of Ti 4p character	0.5	1.8	0.0	0.0	0.1	
total amt of Cl 3p character	9.8	13.5	1.8	1.3	5.4	31.8
total amt of C_5Me_5 character	10.3	27.5	27.8	30.3	22.5	
			$(C_5Me_5)_2ZrCl_2$, **2**			
energy (eV)	−1.73	−0.77	−0.30	0.00	0.11	
total amt of Zr 4d character	71.9	49.2	67.7	63.3	60.3	
total amt of Zr 5p character	0.6	3.2	0.0	0.0	1.8	
total amt of Cl 3p character	9.8	8.2	2.4	2.4	5	27.8
total amt of C_5Me_5 character	17.7	39.4	29.9	34.3	32.9	
			$(C_5Me_5)_2HfCl_2$, **3**			
energy (eV)	−1.41	−0.56	0.11	0.40	0.44	
total amt of Hf 5d character	67.0	45.4	60.9	34.6	50.3	
total amt of Hf 6p character	1.0	2.8	0.4	2.1	0.3	
total amt of Cl 3p character	9.4	5.6	1.8	4.8	2.2	23.8
total amt of C_5Me_5 character	22.6	46.2	36.9	58.5	47.2	

[a] α orbital energies are reported.

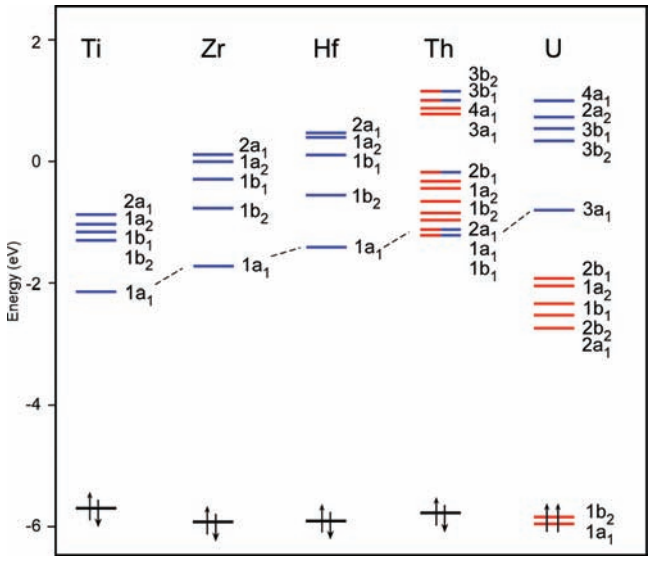

Figure 4. Calculated molecular orbital energy diagram for $(C_5Me_5)_2MCl_2$ (M = Ti, **1**; Zr, **2**; Hf, **3**; Th, **4**; U, **5**) showing orbitals that have primarily *n*d character (blue), primarily 5f character (red), and >10% *n*d and >20% 5f character (half red and blue). For Th and U, although orbital symmetry labels associated with the C_{2v} point group are used to simplify the electronic structure description for $(C_5Me_5)_2MCl_2$ compounds, the optimized structures deviate from pure C_{2v} symmetry.

5. From the C_{2v} orbitals it is easy to see the nature of U−Cl σ- or π-antibonding interactions. The $1a_1$ and $2b_2$ orbitals represent U−Cl π-antibonding interactions that are within the UCl_2 plane, while the $1b_1$, $1a_2$, and $2b_1$ orbitals represent U−Cl π-antibonding interactions that are perpendicular to the UCl_2 plane. The $2a_1$ orbital is U−Cl σ-antibonding. There is no real reason for the pronounced 5-over-2 pattern of 5f-orbital energies, and the stabilization of the $1a_1$ and $1b_2$ 5f-orbitals seen in Figure 4 is likely an artifact of those orbitals being singly occupied in the calculation. For $(C_5Me_5)_2ThCl_2$, **4**, and $(C_5H_5)_2ThCl_2$, **9**, the situation is more complicated due to the near degeneracy of the 5f- and 6d-orbitals and strong 5f−6d hybridization.[56] All 12 of the unoccupied metal-based orbitals contain both 5f and 6d character and span a relatively narrow energy range.

The combination of trends in MO energies from Figure 4, pre-edge peak positions from Figure 1, and peak assignments for transition-metal analogues from Figure 2 provides insight into the pre-edge peak assignments for the Cl K-edge XAS spectra of the actinide compounds. Calculations for $(C_5Me_5)_2UCl_2$ suggest two groupings of 5f-orbitals followed by the a_1 orbital of the 6d manifold. This suggests that the first two peaks in the spectrum of **5** are derived from Cl 1s transitions into 5f-oribitals, and the third peak results from the 6d-orbital of a_1 symmetry. From the MO diagram of Figure 4, we see a smooth increase in d-orbital energetics along the series 3d, 4d, 5d, and 6d. The first peak in the transition element spectra was assigned to transitions into the $1a_1$ d-orbital, and this peak increased in energy from Ti to Zr and Hf as expected from the calculations. Extrapolation of this reasoning to the $(C_5Me_5)_2UCl_2$ spectrum suggests that the third pre-edge peak (2823.44 eV) falls into the region consistent with the 6d virtual orbital. For $(C_5Me_5)_2ThCl_2$, transitions into the lower eight 5f/6d-orbitals, which span only 1.1 and 1.4 eV for $(C_5H_5)_2ThCl_2$ and $(C_5Me_5)_2ThCl_2$, respectively, would correspond to the single pre-edge shoulder in the XAS spectrum, Figure 4, Table 4.

Hybrid DFT Spectral Simulations. To gain more confidence in our pre-edge XAS peak assignments, we turned to electronic structure calculations to simulate the spectra. TD-DFT has been recently applied to simulate Cl K-edge XAS spectra for d-block metallocenes.[43,47,61] The TD-DFT-simulated Cl K-edge XAS for $(C_5Me_5)_2MCl_2$ (Ti, **1**; Zr, **2**; Hf, **3**) are shown in Figure 6. The simulated spectra in Figure 6 have all been shifted by a constant 64.9 eV as described previously[47] and in the Experimental Section. The calculated spectra agree well with the experimental data and predict two pre-edge features for **1** and **2** and three features for **3**, Figure 6. The first pre-edge feature in the Cl K-edge XAS spectra of **1**−**3** is attributed to an electronic excitation from the Cl 1s-orbital into the low-lying $1a_1$ M−Cl π-antibonding d-orbital, Figure 4. The second pre-edge feature of **1** and **2** (Ti, Zr) is attributed to an electronic excitation from the Cl 1s-orbital into the manifold of four higher lying M−Cl σ- and π-antibonding d-orbitals of $1b_2$, $1b_1$, $1a_1$, and $2a_1$ symmetries. Since these four d-orbitals are very close in energy for Ti, Zr, and Hf, individual transitions could not be

Table 4. Orbital Composition (%) for the 12 Primarily 5f- and 6d-Based Orbitals Showing the Calculated Total Amount of Cl 3p Character (%) for the Specified Orbitals in $(C_5R_5)_2AnCl_2$ (M = Th, U; R = H, Me)

$(C_5H_5)_2ThCl_2$, **9**

	MO label												
	68 (LUMO)	69	70	71	72	73	74	75	76	77	78	80	total amt of Cl 3p character (68−75)
energy (eV)	−1.78	−1.68	−1.46	−1.41	−1.19	−1.00	−0.90	−0.71	0.33	0.57	0.58	1.45	
total amt of Th 5f character	60.9	50.4	78.8	78.9	78.6	93.1	83.1	41.3	21.9	22.2	30.2	1.6	
total amt of Th 6d character	13.5	25.3	6.9	3.8	8.3	1.6	10.6	41.7	51.9	37.3	26.3	61.9	
total amt of Cl 3p character	0.8	2.5	0.9	8.6	4.3	3.6	3.2	9.5	3.3	4.8	9.6	10	33.4
total amt of C_5H_5 character	24.7	21.7	13.4	8.7	8.8	1.5	3.0	7.1	22.9	35.5	33.5	26.3	

$(C_5Me_5)_2ThCl_2$, **4**

	MO label												
	108 (LUMO)	109	110	111	112	133	114	115	116	117	118	119	total amt of Cl 3p character (108−115)
energy (eV)	−1.26	−1.20	−0.97	−0.91	−0.65	−0.40	−0.32	−0.17	0.81	0.87	1.01	1.16	
total amt of Th 5f character	52.3	39.4	67.3	76.5	76.9	92.0	85.0	56.9	24.9	43.8	24.0	16.8	
total amt of Th 6d character	22.1	36.5	8.3	7.5	5.8	2.2	8.7	30.3	5.5	17.5	46.1	35.7	
total amt of Cl 3p character	1.2	1.7	0.6	0.0	3.4	2.9	2.2	5.8	5.3	9.6	1.6	0.6	17.8
total amt of C_5Me_5 character	24.1	22.3	23.7	16.0	13.9	2.5	3.8	6.4	64.1	28.3	28.1	46.9	

$(C_5H_5)_2UCl_2$, **10**

	MO label												
	primarily 5f							primarily 6d					
	68 (SOMO − 1)	69 (SOMO)	70 (LUMO)	71	72	73	74	75	76	77	78	79	total amt of Cl 3p character (68−75)
energy (eV)	−6.84	−6.51	−3.32	−3.15	−2.90	−2.77	−2.56	−1.15	−0.13	0.10	0.49	1.18	
total amt of U 5f character	92.7	70.6	92.4	87.3	89.8	86.7	85.0	4.4	7.3	4.2	4.2	1.8	
total amt of U 6d character	1.3	4.6	1.7	1.8	2.3	4.4	5.5	59.1	31.4	51.9	38.7	34.8	
total amt of Cl 3p character	1.2	9.6	0.9	2.6	2.8	2.7	2.0	9.1	6.8	1.8	2.6	44.7	30.8
total amt of C_5H_5 character	4.7	15.1	5.0	8.3	5.0	6.2	7.5	26.8	53.8	42.1	54.5	18.7	

$(C_5Me_5)_2UCl_2$, **5**

	MO label												
	primarily 5f							primarily 6d					
	108 (SOMO − 1)	109 (SOMO)	110 (LUMO)	111	112	133	114	115	116	117	118	119	total amt of Cl 3p character (108−115)
energy (eV)	−5.93	−5.86	−2.73	−2.53	−2.35	−2.07	−1.93	−0.81	0.35	0.55	0.74	0.99	
total amt of U 5f character	44.1	12.3	89.2	88.4	88.4	84.5	87.1	2.5	10.9	4.9	5.0	3.7	
total amt of U 6d character	6.2	2.9	2.9	2.9	3.3	5.0	4.3	61.7	30.1	18.7	37.5	29.9	
total amt of Cl 3p character	3.6	2.1	1.5	2.5	2.7	1.5	1.8	7.3	1.3	2.4	1.9	1.3	23
total amt of C_5Me_5 character	45.1	80.5	6.4	6.2	5.6	8.6	6.7	27.9	9.3	60.4	55.4	65.1	

resolved experimentally. These XAS peak assignments are essentially identical to those previously reported for the $(C_5H_5)_2MCl_2$ analogue spectra of **6**−**8** (Ti, Zr, Hf).[47] In addition, the simulated and experimental XAS peak separation of 1.21 eV for **2** is similar to the theoretical prediction of 1.1 eV. For **3**, the three peaks are separated by 1.07 and 0.63 eV, which is close to the 1.1 and 0.6 eV prediction. The most significant difference between the electronic structure calculations and the experimental data is that the theory in all cases predicts a decrease in M−Cl orbital mixing for $(C_5Me_5)_2MCl_2$ vs $(C_5H_5)_2MCl_2$. However, experimentally, no appreciable change in M−Cl covalency was observed, despite the differences in electron-donating ability of the ancillary cyclopentadienyl ligands.

For computational simulation of actinide XAS spectra, we employed two different techniques (see the Experimental Section). For the closed-shell Th systems **4** and **9**, we used the TD-DFT approach as in the transition-metal analogues. TD-DFT for molecules with open-shell ground states is not presently available in Gaussian 03. Therefore, for open-shell U systems **5** and **10**, we examined an approximation to the DFT linear response methodology that consists of calculating transition dipoles among ground-state molecular orbitals (see the Experimental Section). This approach gave results essentially identical to those of the TD-DFT calculations conducted on **1**−**4** and **6**−**9**. To facilitate comparison of calculated spectral transitions with experimental data for actinide systems via these two approaches, we set the energy of the first calculated 6d peak to be that of the experimentally determined 6d peak. This corresponds to an energy shift of 65.9 eV for Th and 63.4 eV for U. In our view, this gives a more satisfying means to make comparison between calculated and experimental spectra and illustrates our use of spectral simulation to provide guidance for interpreting the pre-edge regions of the spectra.

The calculated Cl K-edge X-ray absorption spectrum of $(C_5Me_5)_2ThCl_2$, **4**, predicts only one pre-edge feature corresponding to transitions to the lower group of nearly degenerate and heavily mixed 5f- and 6d-orbitals, Figure 7. This prediction

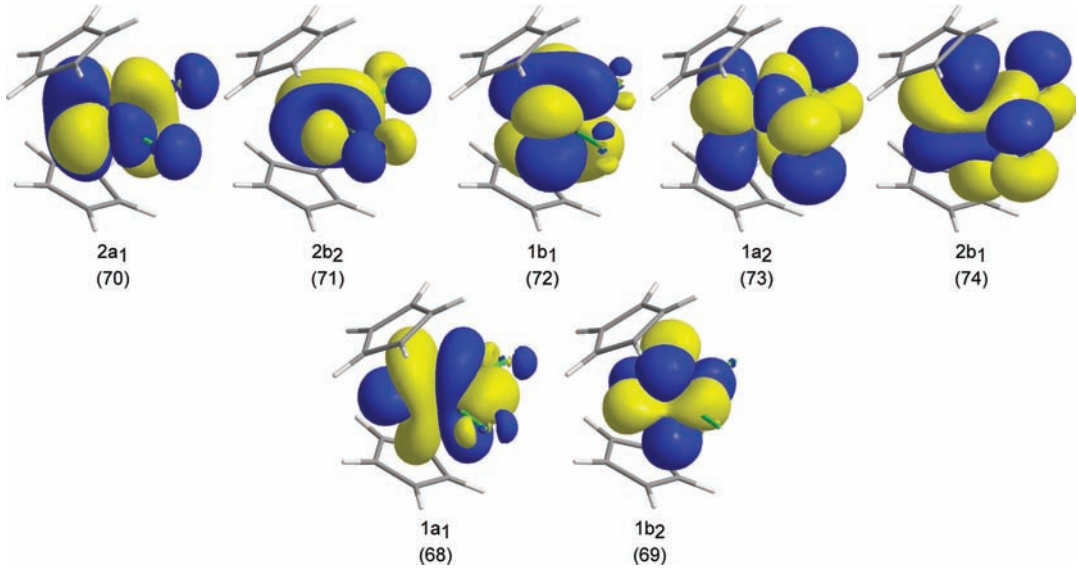

Figure 5. Relevant Kohn−Sham orbitals that have primarily 5f character for $(C_5H_5)_2UCl_2$ constrained to C_{2v} symmetry. Only the U 5f and Cl 3p contributions are shown.

is consistent with experimental spectra containing a single pre-edge shoulder on the rising edge of the white line. These results indicate that the pre-edge shoulder in the experimental Cl K-edge XAS spectrum of **4** is attributed to Cl 1s electron excitations into the manifold of eight metal-based 5f/6d Th−Cl antibonding orbitals (Figure 4).

Due to the open-shell ground state of $(C_5Me_5)_2UCl_2$, **5**, which contains two unpaired 5f electrons, the XAS spectrum was simulated using a dipole transition calculation instead of TD-DFT. For **5**, the dipole transition simulated spectrum is in good agreement with the experimental data as shown in Figure 7. Both calculated and experimental spectra show three pre-edge features. The first feature is attributed to a Cl 1s electron excitation into the $1a_1$ and $1b_2$ partially occupied 5f-orbitals, Figures 4 and 7.[83] The second feature is attributed to electronic excitations from Cl 1s-orbitals into a manifold of five higher lying 5f-orbitals, while the third feature involves electronic excitations into the $3a_1$, primarily 6d-orbital with U−Cl π-antibonding character. These data suggest that the spectrum of $(C_5Me_5)_2UCl_2$ differs from the transition-metal spectra of **1**−**4** in that the spectrum of **5** contains distinct 5f and 6d components. Comparing the Cl K-edge XAS spectra for $(C_5Me_5)_2MCl_2$ with M = Ti, Zr, Hf, and U provides confidence in these assignments since it shows that descending the periodic table results in successive energy increases for the 3d, 4d, 5d, and 6d 1s → a_1 transitions, which are 2821.31, 2822.41, 2822.86, and 2823.44 eV, respectively (Figures 4 and 7). Since DFT calculations predict that transitions into the remaining higher lying 6d-orbitals are even higher in energy and close to the white line, they are not likely to be experimentally resolved. As a result, their contribution to covalency in the U−Cl bond derived from XAS is neglected in the following discussions.

Overall, the DFT calculations are in agreement with the experimental Cl K-edge XAS spectrum of $(C_5Me_5)_2UCl_2$, especially in the prediction of three pre-edge features, and aid in our interpretation of these features arising from Cl 1s transitions into both 5f- and 6d-orbitals. However, theoretical calculations overestimate the magnitude of 5f-orbital interaction with Cl ligands and the associated energy separation between 5f peaks. The calculated energy separation between 5f peaks is 3.13 eV compared to the 0.82 eV experimental value. The experimentally determined 1.45 eV 5f/6d-orbital energy gap is slightly larger than the calculation suggests, which is 1.12 eV. These differences are likely related to the choice of functional and lack of inclusion of spin−orbit and multiplet effects. Finally, comparison of **4** and **5** provides additional insight into electronic structure changes from left to right within the actinide series. In this case, transitions involving molecular orbitals that contain 5f character are lower in energy for $(C_5Me_5)_2UCl_2$ than for $(C_5Me_5)_2ThCl_2$, which is consistent with the previously reported Xα-SW molecular orbital calculations performed on $(C_5H_5)_3M$ (M = U, Np, Pu, Am, Cm, Bk, Cf)[84] and $(C_8H_8)_2M$ (M = Th, Pa, U, Np, Pu).[85]

Concluding Remarks

The comparison of experimental and simulated Cl K-edge XAS spectra of $(C_5Me_5)_2MCl_2$ (M = Ti, Zr, Hf, Th U, **1**−**5**, respectively) offers a unique opportunity to evaluate the relative roles of the valence f- and d-orbitals in M−Cl bonding in the class of bent metallocene dichloride complexes. The experimental results for transition elements indicate that the amount of Cl 3p mixing with metal-based orbitals follows the trend of 25%, 23%, and 22% for **1**, **2**, and **3**, respectively (Table 2). Although these experimental values are nearly indistinguishable, the calculated values, while smaller in magnitude, show essentially the same trend (16%, 14%, 12%) and suggest that covalency decreases in the order **1** > **2** > **3**. For $(C_5Me_5)_2UCl_2$, **5**, the experimental results indicate that the amount of Cl 3p mixing with metal-based orbitals is only 9% (Table 2), but this determination excludes contributions from higher lying 6d-orbitals that cannot be experimentally resolved. The calculated amount of Cl 3p mixing for this same set of metal-based orbitals (the 5f and 6d $1a_1$) is 12%.

(83) Because of the open-shell nature of the f^2 system, the top two α molecular orbitals are singly occupied.

(84) Strittmatter, R. J.; Bursten, B. E. *J. Am. Chem. Soc.* **1991**, *113*, 552.
(85) Boerrigter, P. M.; Baerends, E. J.; Snijders, J. G. *Chem. Phys.* **1988**, *122*, 357.

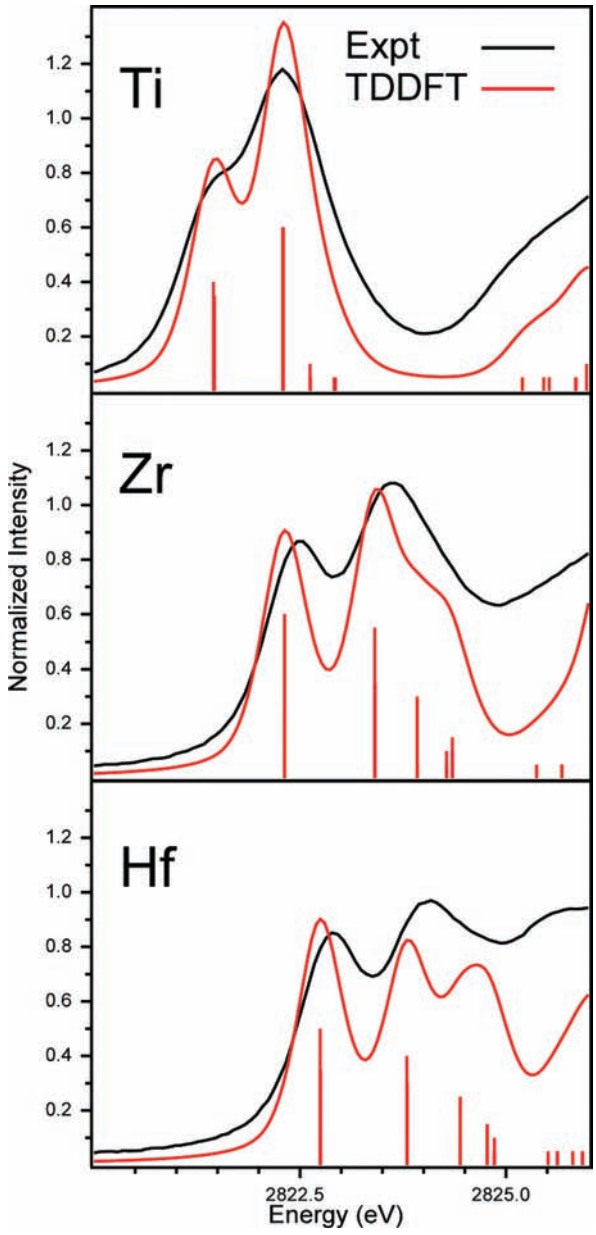

Figure 6. Cl K-edge X-ray absorption spectra (black lines), TD-DFT-calculated spectra (red lines), and calculated transitions (red bars) for polystyrene films of $(C_5Me_5)_2MCl_2$ (M = Ti, **1**; Zr, **2**; Hf, **3**). The height of the red bars represents the calculated oscillator strength for the individual transitions.

While the experimental data preclude a comparison of all five d-orbitals within this series, we can compare the calculated values. If we include all 12 5f and 6d metal-based orbitals in the theoretical analysis, then we arrive at a total amount of Cl 3p mixing with metal-based orbitals of 15%. The theoretical calculations allow us to break this down into 8% Cl mixing with 5f-orbitals and 7% Cl mixing with 6d-orbitals. From this theoretical analysis we find a clear trend of decreasing amount of Cl 3p interaction with d-orbitals of 16%, 14%, 12%, and 7% (Tables 3 and 4) for **1**, **2**, **3**, and **5**, respectively. Thus, covalency in M−Cl bonding from d-orbital interactions with Cl 3p-orbitals follows the trend Ti > Zr > Hf > U. For U, we superimpose weak 5f-orbital interactions onto this d-orbital picture of M−Cl bonding. The calculations appear to overemphasize the amount of 5f-orbital participation in M−Cl bonding, where we find 4% Cl 3p mixing experimentally and 8% Cl 3p

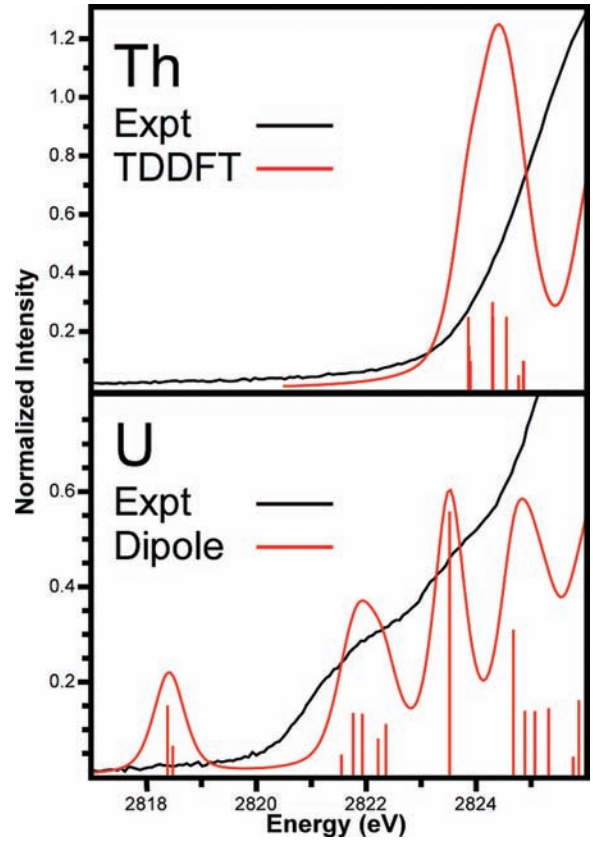

Figure 7. (Top) Comparison of the experimental Cl K-edge X-ray absorption spectrum for $(C_5Me_5)_2ThCl_2$, **4**, (black line) to the simulated TD-DFT spectrum (red line). (Bottom) Comparison of the experimental Cl K-edge X-ray absorption spectrum for $(C_5Me_5)_2UCl_2$, **5**, (black line) to the simulated dipole transition spectrum (red line). In both comparisons, the calculated transitions are indicated below the spectrum as red bars whose height represents the calculated oscillator strength for the individual transitions.

mixing from theoretical calculations. Overall, these covalency trends suggest greater 6d-orbital participation than 5f-orbital participation in M−Cl bonding and are similar to the trends revealed by previously reported measurements that used gas-phase photoelectron spectroscopy to probe the occupied orbitals of metallocene complexes.[62−65]

The changes in d-orbital covalency among 3d, 4d, 5d, and 6d elements can be readily understood from simple perturbation molecular orbital theory. It is well-known that the magnitude of orbital interaction is proportional to the square of the orbital overlap between two centers and inversely proportional to the energy gap between them.[86] For a common ligand such as Cl, the energy gap between Cl 3p- and metal *n*d-orbitals increases as we progress the series 3d, 4d, 5d, and 6d because the metal-based orbitals rise in energy with increasing principal quantum number, Figure 4. The increase in the energy gap gives rise to lower covalent mixing along the series 3d, 4d, 5d, and 6d. The application of Cl K-edge XAS has provided a unique opportunity to evaluate the electronic structure, bonding, and covalency in metallocene dichlorides and seems exceptionally well suited for study of metal−ligand bonding in other important actinide systems. Current efforts are under way to expand the use of ligand K-edge XAS and DFT to the transuranic elements.

Acknowledgment. We are grateful to S. DeBeer George for helpful discussions, and insights from several anonymous reviewers. This work was supported at Los Alamos by the Division of

Chemical Sciences, Geosciences, and Biosciences, Office of Basic Energy Sciences, U.S. Department of Energy, a Glenn T. Seaborg Institute Postdoctoral Fellowship (P.Y.), and a Frederick Reines Postdoctoral Fellowship (S.A.K.). Portions of this research were carried out at the Stanford Synchrotron Radiation Lightsource, a national user facility operated by Stanford University on behalf of the U.S. Department of Energy, Office of Basic Energy Sciences. Los Alamos National Laboratory is operated by Los Alamos National Security, LLC, for the National Nuclear Security Administration of the U.S. Department of Energy under Contract DE-AC52-06NA25396.

Supporting Information Available: X-ray absorption spectra, structural parameters, and summaries of the DFT calculations. This material is available free of charge via the Internet at http://pubs.acs.org.

JA9015759

(86) Albright, T. A.; Burdett, J. K.; Whangbo, M. *Orbital Interactions in Chemistry*; Wiley and Sons: New York, 1985; 464 pp.